Article

Lignin alkali regulated interfacial polymerization towards ultra-selective and highly permeable nanofiltration membrane

Wentian Zhang[1,2], Shanshan Zhao [1,2] ✉, Haiyun Li[1,2], Cunxian Lai[1,2], Shangwei Zhang[3], Wu Wen[4], Chuyang Y. Tang [5] ✉ & Fangang Meng [1,2] ✉

Thin-film composite polyamide (TFC PA) membranes hold promise for energy-efficient liquid separation, but achieving high permeance and precise separation membrane via a facile approach that is compatible with present manufacturing line remains a great challenge. Herein, we demonstrate the use of lignin alkali (LA) derived from waste of paper pulp as an aqueous phase additive to regulate interfacial polymerization (IP) process for achieving high performance nanofiltration (NF) membrane. Various characterizations and molecular dynamics simulations revealed that LA can promote the diffusion and partition of aqueous phase monomer piperazine (PIP) molecules into organic phase and their uniform dispersion on substrate, accelerating the IP reaction and promoting greater interfacial instabilities, thus endowing formation of TFC NF membrane with an ultrathin, highly cross-linked, and crumpled PA layer. The optimal membrane exhibited a remarkable water permeance of 26.0 L m^{-2} h^{-1} bar^{-1} and Cl$^-$/SO$_4^{2-}$ selectivity of 191.0, which is superior to the state-of-the-art PA NF membranes. This study provides a cost-effective scalable strategy for fabricating ultra-selective and highly permeable NF membrane for precise ion-ion separation and small organic compounds removal.

Thin-film composite polyamide (TFC PA) nanofiltration (NF) membrane has demonstrated profound potential in supplying clean water from unconventional sources such as wastewater, seawater and brackish water, due to its prominent solute-water and solute-solute selectivity[1–3]. Generally, PA NF membrane is fabricated by interfacial polymerization (IP) upon a porous substrate, where the amine monomers in an aqueous phase diffuse into an organic solvent phase and polymerize with acyl chloride monomers at the aqueous-organic interface[4–6]. However, in a conventional IP process, the distribution and diffusion of monomers are uncontrollable, resulting in an undesired PA layer that lacks precise selective capability and high water permeance[7,8]. In addition, enhancing the performance of PA NF membranes often encounters a trade-off problem: improving

selectivity and water permeance simultaneously proves challenging, ascribing to the intrinsic properties of PA layer. Typically, increase in selectivity requires a PA layer with higher degree of cross-linking, which in turn increases water transport resistance and thereby reduces water permeance. Therefore, understanding the mechanism of IP process and effectively regulating IP reaction are critical for breaking the trade-off phenomenon for promoting PA NF membrane performance to address the increasingly growing water scarcity issues.

Generally, the porous support used in IP process contains randomly distributed pores on the surface and it has week interaction with amine monomers, leading to the discontinuous and non-uniform distribution and limited storage of amine monomers on substrate. This results in the formation of a thick PA layer with wide pore size

[1]School of Environmental Science and Engineering, Sun Yat-sen University, Guangzhou, China. [2]Guangdong Provincial Key Laboratory of Environmental Pollution Control and Remediation Technology, Guangzhou, China. [3]Advanced Interdisciplinary Institute of Environment and Ecology, Beijing Normal University, Zhuhai, China. [4]Instrumentation and Service Center for Science and Technology, Beijing Normal University, Zhuhai, China. [5]Department of Civil Engineering, The University of Hong Kong, Hong Kong SAR, China. ✉e-mail: zhaoshsh7@mail.sysu.edu.cn; tangc@hku.hk; mengfg@mail.sysu.edu.cn

distribution. In addition, recent studies have emphasized that controlling stoichiometric equilibrium or diffusion kinetics of reaction monomers is important to achieve high performance PA NF membranes[9,10]. Therefore, great efforts have been made to regulate IP process for improving the perm-selectivity of NF membranes in the past decade, including free-standing membrane fabrication[11,12], building interlayer on substrate[13–15] or involving nanomaterials additives in aqueous solution[16], etc. These approaches either improve the uniform dispersion of amine monomers, or regulate their diffusion rates for fabricating thinner, defect-free, and/or crumpled PA layer. Despite the performance improvement by above approaches, the weak mechanical strength of free-standing PA layer makes it impossible for actual application, and redundantly modification steps of involving interlayer or nanomaterials are difficult to be compatible with existing manufacturing line and cause additional carbon footprint. Undoubtedly, seeking a simple method to achieve simultaneously uniform distribution of amine monomers and regulating IP reaction rate is of great significance to develop high performance NF membrane.

Herein, we report a facile and highly practical method using renewable lignin alkali (LA) as an aqueous solution additive to regulate IP reaction to achieve ultra-selective and highly permeable NF membrane. Lignin, produced by plant cells in the plant growth process, can bind cells together and enhance the mechanical strength of plant cells and tissues[17,18]. Inspired from lignification during plant growth process, we expect that the water soluble LA molecules can be homogeneously adsorbed onto polysulfone substrate surface due to hydrophobic-hydrophobic interaction and π-π stacking[19], while also providing abundant hydrophilic functional groups (-OH, -OCH$_3$, -SH) for interacting with piperazine (PIP) molecules through electrostatic or hydrogen bonding. Moreover, since LA molecules have both hydrophobic benzene ring and hydrophilic functional groups, they may affect the interfacial tension of aqueous-organic interface as surfactants do. These two aspects can improve the uniform distribution of PIP molecules on the substrate surface, and increase the diffusion rate of PIP across the aqueous-organic interface and its partition in organic phase, contributing to the formation of an ultrathin, highly cross-linked and crumpled PA separation layer. The optimized membrane shows a remarkable pure water permeance of 26.0 L m^{-2} h^{-1} bar^{-1} and Cl$^-$/SO$_4^{2-}$

selectivity of 191.0, which is superior to the state-of-the-art PA NF membranes reported both in literature and in market. The mechanisms of LA regulation are also studied in detail through experiments, a series of advanced characterizations, molecular dynamics (MD) simulations, and Density Functional Theory (DFT) calculations. The addition of LA in aqueous phase solution is compatible with the present industrial production line, which offers a simple and facile approach for IP process regulation. Furthermore, abundant LA is readily available from alkaline paper pulp waste without additional cost. Our work provides a cost-effective scalable approach for fabricating robust TFC membranes such as NF, reverse osmosis, and forward osmosis.

Results

Fabrication and characterization of LA regulated TFC membranes

The performance of TFC NF membrane is mainly determined by the thickness and nanoscale homogeneity of PA layer, which can be tuned during IP process. Through controlling the initial dispersion state of amine monomers and their diffusion behaviors from aqueous phase to organic phase can significantly regulate the formation and characteristics of PA nanofilm. Herein, we introduced LA as an additive into PIP aqueous solution in order to regulate PIP distribution and its reaction with trimesoyl chloride (TMC) for fabricating a robust NF membrane with ultrathin, highly cross-linked and crumpled PA layer, which is defined as LA-TFC (Fig. 1). For comparison, a conventional IP process was employed to prepare the control TFC (C-TFC) membrane using PIP solution without LA.

As observed by scanning electron microscopy (SEM) and atomic force microscopy (AFM) (Fig. 2 and Supplementary Fig. 1), the C-TFC and LA-TFC membranes exhibited obviously different surface morphologies. The C-TFC membrane presented a smooth and conventional nano-nodular PA structure, while the LA-TFC membrane had a crumpled structure. It has been reported that the crumpled structure can increase the water collection area thus efficiently improving the membrane permeability[20,21]. As shown in Supplementary Fig. 1, the area of crumpled structure increased with LA concentration increasing, and the wrinkles distributed the most uniformly when LA concentration was 0.75 wt%. The root-mean-square roughness (RMS) results reveal
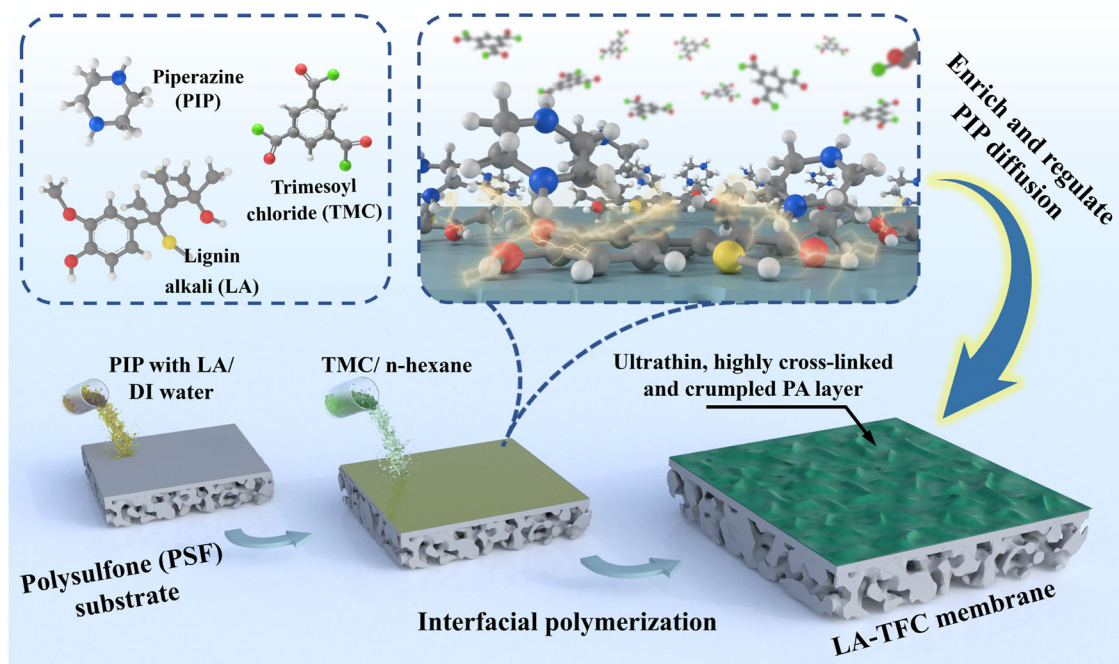

Fig. 1 | Membrane fabrication process. Schematic illustration of fabrication process of lignin alkali-thin film composite (LA-TFC) membrane.
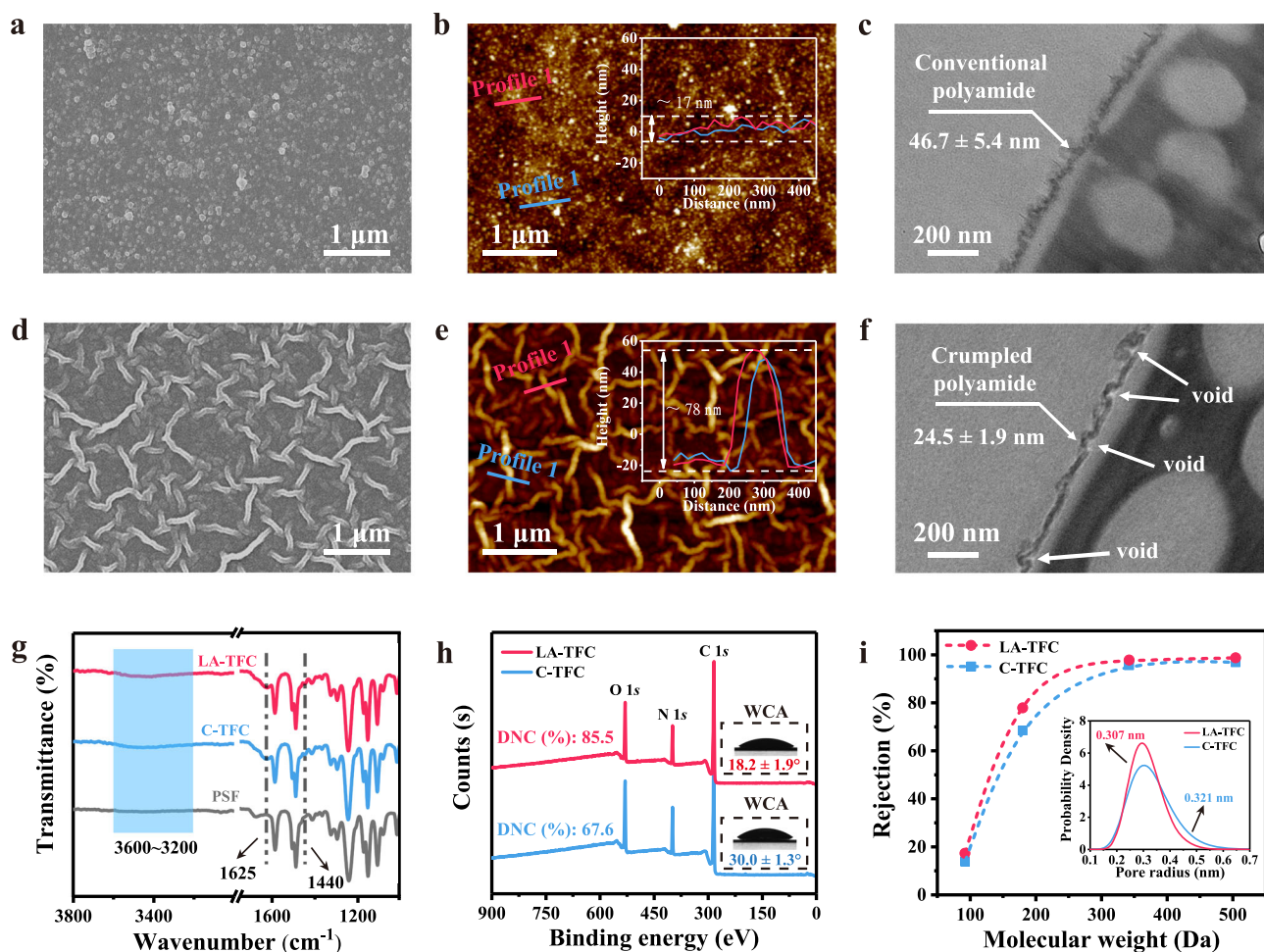
Fig. 2 | Morphologies and physicochemical properties of different TFC membranes. a, d SEM and **b, e** AFM images of surface morphologies of control-thin film composite (C-TFC) and lignin alkali-thin film composite (LA-TFC) membranes, respectively. **c, f** TEM images of cross-section morphologies of C-TFC and LA-TFC membranes, respectively. **g** ATR-FTIR spectra of polysulfone (PSF) and TFC membranes. **h** XPS survey scan spectra of TFC membranes. **i** MWCO of TFC membranes. Inserts in (**b, e**) are height profiles of the corresponding PA nanofilms, inserts in (**h**) are degree of network cross-linking (DNC) and water contact angles (WCAs) of C-TFC and LA-TFC membranes, and inserts in (**i**) are pore size distributions of C-TFC and LA-TFC membranes, respectively. The concentration of LA for LA-TFC membrane preparation was 0.75 wt%.

that the LA-TFC membrane with crumpled PA structure had rougher surface than that of C-TFC membrane. The average height of wrinkles was ~78 nm, which was significantly higher than those nano-nodules (~17 nm) (Fig. 2b and e). Transmission electron microscopy (TEM) measurements were further performed to investigate the thickness and internal structures of different PA layers. Compared with C-TFC membrane, the LA-TFC membrane presented a thinner PA layer, and abundant voids were observed between the crumpled PA nanofilm and polysulfone (PSF) substrate, indicating that the crumpled structures are hollow inside (Fig. 2f). The above results demonstrate that the addition of LA in aqueous phase solution can regulate the reaction of PIP and TMC at the aqueous-organic interface during IP process, with the resulting thinner and crumpled PA layer achieving greatly enhanced water permeability (see the Section on "Separation performance of LA-TFC membranes").

The surface functional groups of TFC membranes were measured using Fourier transform infrared spectrometer with attenuated total reflectance mode (ATR-FTIR). Both C-TFC and LA-TFC membranes have new peaks at 1440 cm^{-1} and 1625 cm^{-1} (Fig. 2g) in comparison with PSF substrate, corresponding to O-H bending vibration and C=O stretching vibration of amide I, which are the typical peaks of PA nanofilm. Additionally, a broad peak at 3200–3600 cm^{-1} is ascribed to the O-H stretching vibration of carboxyl groups[22]. The surface elemental

compositions of TFC membranes were investigated using X-ray photoelectron spectrometer (XPS) (Fig. 2h and Supplementary Table 1). Compared with PSF substrate, the sulfur contents of both TFC membranes decreased while the nitrogen contents increased due to the formation of PA nanofilms. Moreover, the LA-TFC membrane possessed denser PA layer with a higher degree of network cross-linking (DNC) (85.5%) than that of C-TFC membrane (67.5%) calculated based on the O/N ratios[23]. The molecular weight cut-off (MWCO) of TFC membranes was determined by measuring the rejections of a series of neutral organic solutes (i.e., raffinose, sucrose, glucose, and glycerol) (Fig. 2i). Compared with C-TFC membrane, the LA-TFC membrane had a smaller MWCO (227 Da vs 281 Da) and a narrower pore size distribution, and meanwhile, the mean pore radius of LA-TFC membrane was also smaller than that of C-TFC membrane (0.307 nm vs 0.321 nm) due to its higher DNC, which is more appropriate for high selective separation applications.

In order to further investigate the chemical states of membrane surface compositions, high-resolution C 1s, N 1s, and O 1s XPS spectra were employed (Supplementary Fig. 2 and Supplementary Table 2). The C 1s spectra are divided into three peaks including 284.6 eV (aliphatic/aromatic C-H or C-C bonds), 286.0 eV (C-N), and 288 eV (amide O-C=N and carboxyl O-C=O groups). The N 1s spectra include two peaks at 399.5 eV and 401.7 eV, corresponding to N-C=O and R-N-H, respectively. The O 1s spectra can be divided into two components at

530.6 eV (O=C-N) and 532.6 eV (O-C=O)[22]. As observed from Supplementary Table 2, both the ratios of unreacted amine and carboxyl groups on LA-TFC membrane (1.8% and 9.4%) were lower than those on C-TFC membrane (4.3% and 13.4%), implying that there existed more amide bonds in PA nanofilm of LA-TFC membrane due to its higher DNC. Furthermore, the concentrations of carboxyl groups on these two membrane surfaces were also determined using a cationic dye (toluidine blue O, 270 g/mol) adsorption-desorption technique (Supplementary Fig. 3). The results demonstrate that the amount of carboxyl groups on LA-TFC membrane surface was less than that on C-TFC membrane. This is consistent with the higher DNC of LA-TFC membrane. The surface wettability of TFC membranes was also investigated. The water contact angles (WCAs) of LA-TFC and C-TFC membranes were 18.2° and 30.0°, respectively (the insert in Fig. 2h). Despite that the LA-TFC membrane had lower content of hydrophilic carboxyl groups, it exhibited better wettability, possibly ascribing to its increased surface roughness (Supplementary Fig. 1).

Regulating mechanisms of LA on the PA nanofilm formation

The formation of PA nanofilm is considered to be a diffusion-reaction process including two steps. First, PIP molecules diffuse from aqueous phase to organic phase and react with TMC to form the incipient PA layer. Then, the following PIP molecules diffuse slowly across the incipient PA layer to form the final denser PA nanofilm[24,25]. The surface morphology of PA nanofilm is believed to be closely associated with the interfacial instability[26–28]. In general, increased amine monomer supply and enhanced reaction conditions could result in surfaces with greater roughness.

In this study, LA molecules containing both hydrophobic and hydrophilic moieties that suggest surfactant-like behavior, can be easily gathered at the aqueous-organic interface (Fig. 3a and Supplementary Fig. 4b), causing a sharp decrease in the interfacial tension (Supplementary Fig. 5). The reduced interfacial tension can decrease the energy barrier of PIP diffusion from aqueous phase to organic phase as evidenced by MD simulation (5.54 kJ/mol with presence of LA while 7.03 kJ/mol without LA, Fig. 3b), which can facilitate the diffusion of PIP across the aqueous-organic interface (Supplementary Fig. 6). Furthermore, the partition coefficient of PIP in hexane and aqueous phases was also increased (Fig. 3c). These would enhance the effective supply of PIP monomers into organic phase and promote the reaction rate of PIP with TMC (Fig. 3d and Supplementary Fig. 7), thus resulting in greater interfacial instabilities and promoting the formation of thinner and denser PA layer with crumpled structure[29–31]. We also compared the LA impacts on the morphologies with other surfactants such as sodium dodecyl sulfonate (SDS) and cetyltrimethyl ammonium bromide (CTAB). We found that crumpled structure only appeared when SDS with a lower concentration (0.25 critical micelle concentration (CMC)) was involved, and the addition of CTAB cannot form a crumpled structure under various concentrations (Supplementary Fig. 8). This result shows that LA has a greater advantage in increasing the water permeance by significantly increasing the membrane permeation area. Furthermore, the PIP diffusion in the aqueous phase bulk solution stored in the membrane pores might be limited by LA as proved by nuclear magnetic resonance (NMR) measurement (Supplementary Fig. 9) and MD simulation (mean square displacement (MSD) result in Supplementary Fig. 10 and PIP diffusion coefficient result in Fig. 3e), which might also contribute to the formation of thinner PA layer[32].

In addition, LA could improve the uniform distribution of PIP monomers on substrate. Since the LA molecules have hydrophobic benzene ring and hydrophilic functional groups such as phenolic hydroxyl, methoxy ether, and alcohol hydroxyl, they can be uniformly adsorbed onto the PSF substrate surface as evidenced by the observation of distinct and uniformly dispersed brown areas on LA adsorbed substrate (Fig. 3f). Similarly, PIP can be evenly dispersed on the substrate surface through attractive forces between PIP and hydrophilic

functional groups of LA as proved by XPS analyses (Supplementary Table 4). The results of the radial distribution function (RDF) analysis from MD simulation show that the PIP molecule is more inclined to be in close proximity to the oxygen-containing functional groups of LA molecule (Supplementary Fig. 11b). This could be attributed to the fact that the secondary amine functional groups of PIP readily form hydrogen bonds with these groups in a water environment, resulting in a stronger attractive effect. The higher binding energy between LA and PIP compared to PSF and PIP indicates a greater affinity of LA for PIP molecules (Supplementary Fig. 11c, d). The LA promoting the uniform distribution of PIP molecules on the substrate surface is conducive to the formation of PA layer with more uniform pore size.

Furthermore, since LA molecules contain phenolic hydroxyl groups, we also investigated whether LA participated in IP reaction, because previous reports have indicated that polyphenols can react with TMC to fabricate polyester NF membranes[33,34]. Typically, the preparation of polyester membranes involves extended IP reaction time to ensure membrane integrity. Remarkably, even with a brief IP reaction time of 10 s, the crumpled structure can be observed (Supplementary Fig. 12). Additionally, the membrane achieved a Na_2SO_4 rejection rate of 98.0%, whereas the polyester membranes usually exhibit much lower salt rejection rates, around 10–20%[35,36]. The smaller and more reactive PIP can over-compete the bulky and less reactive LA to diffuse into the organic phase and react with TMC. DFT calculations also show that the reaction energy barrier between the acyl chloride and secondary amine groups in PIP (16.47 kcal/mol) is much smaller than that between the acyl chloride and phenolic hydroxyl groups of LA (28.8 kcal/mol) (Fig. 3h, i), indicating that PIP will preferentially react with TMC when its amount is sufficient. In addition, the ATR-FTIR results show that there was no stretch vibration peak of ester group C=O at 1740 cm⁻¹ in both C-TFC and LA-TFC membranes (Supplementary Fig. 13) and the surface SEM image of LA alone reacting with TMC (LA-TMC) membrane revealed no significant difference with that of PSF substrate (Supplementary Fig. 14), indicating that LA alone did not effectively react with TMC.

In summary, despite the reduced PIP diffusion in the aqueous phase bulk solution, LA can decrease the energy barrier of PIP diffusion from aqueous phase to organic phase, increase the partition of PIP in organic phase and promote more amount of PIP uniformly absorbed onto porous substrate. These combined effects would enhance the effective supply of PIP monomers into the organic phase, consequently accelerating IP reaction and promoting greater interfacial instabilities to facilitate the formation of a denser PA layer with more crumpled surface[37], as illustrated in the Fig. 3g. Moreover, ascribing to the higher amount of PIP participating into initial IP process when LA existing, the formation of denser incipient PA layer would further retard subsequent diffusion of PIP, thus endowing LA-TFC membrane with thinner PA nanofilm. Through the above regulation mechanisms, the resultant LA-TFC membrane has ultrathin, highly cross-linked, and crumpled PA layer.

Separation performance of LA-TFC membranes

The effects of LA concentration on the separation performances of LA-TFC membranes were systematically investigated, and the results are shown in Fig. 4. All LA-TFC membranes exhibited higher pure water permeance (PWP) in comparison with C-TFC membrane. The PWP of LA-TFC membranes increased with an increment in LA concentration from 0.00 to 0.75 wt%. However, when the LA concentration was further increased to 1.00 wt%, a slight reduction in PWP was observed. Notably, the LA$_{0.75}$-TFC membrane exhibited the highest PWP of 26.0 L m⁻² h⁻¹ bar⁻¹, which surpassed that of C-TFC membrane by a factor of 3.6-fold magnification. Usually, smaller MWCO and narrow pore size distribution might result in higher water transport resistance. However, in our study, although the MWCO of LA-TFC membrane is smaller than that of C-TFC membrane (Fig. 2), the LA-TFC membrane still has ultrahigh PWP due to its thinner and crumple PA nanofilm with
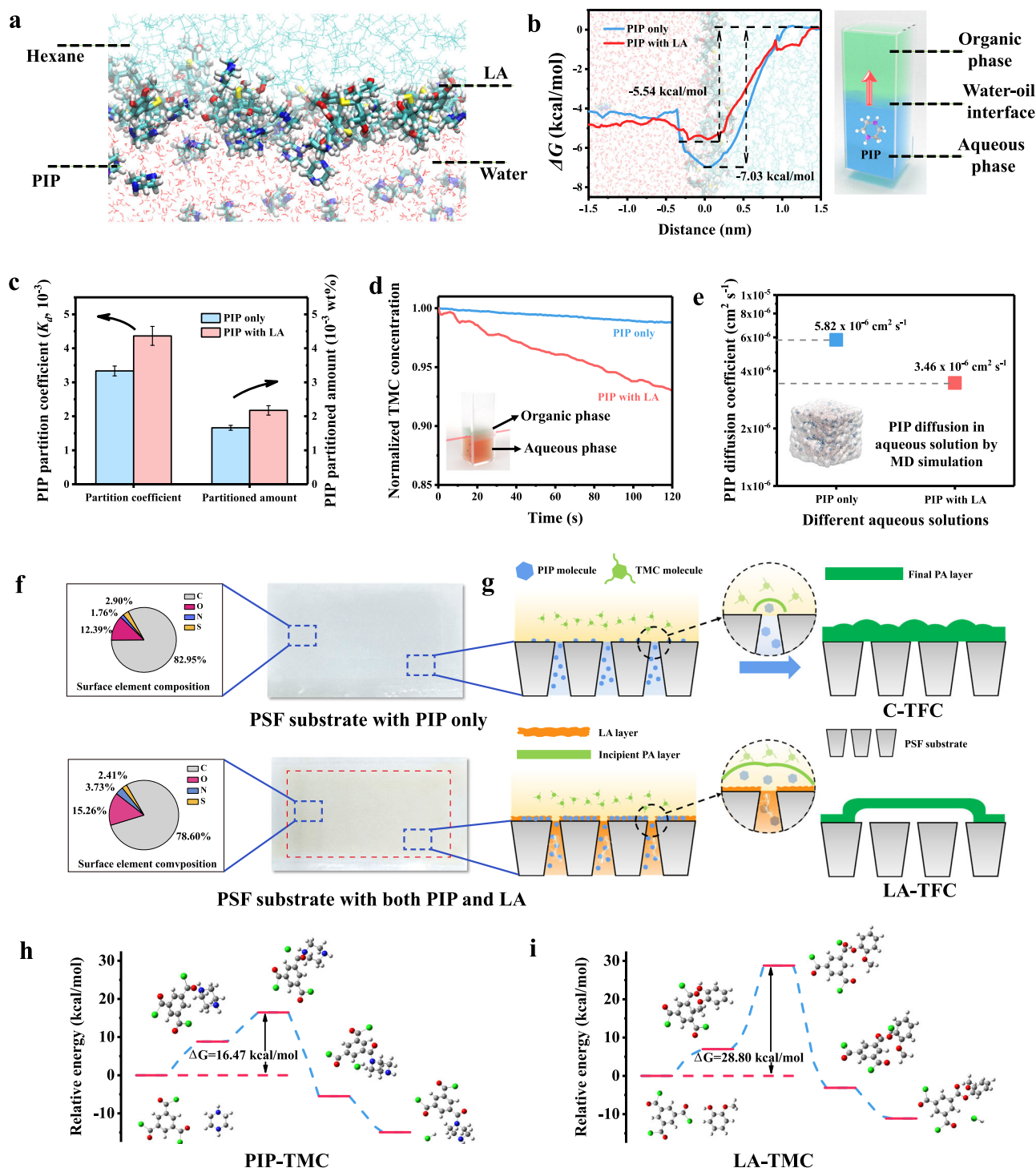
Fig. 3 | The mechanisms of lignin alkali (LA) in fabrication of thin film composite (TFC) membranes. a The snapshot of the water-hexane interface of piperazine (PIP) solution with LA after 10 ns molecular dynamics (MD) simulation (Supplementary Fig. 4). **b** The free energy (ΔG) of PIP versus the z coordinates perpendicular to the water-hexane interface (right image is the schematic illustration of pulling the PIP from the aqueous phase to the organic phase). **c** The partition coefficient of PIP in organic and aqueous phases and PIP partitioned amount in hexane (the partition coefficient of PIP was calculated by Eq. (8), and PIP partitioned amount was determined by UV spectrophotometer characterization). **d** The normalized concentration of trimesoyl chloride (TMC) in hexane over reaction time during the interfacial polymerization (IP) process (the initial concentration of TMC is 0.05 wt%). **e** The diffusion rate of PIP in aqueous phase bulk solution by MD simulation (the insert represents the simulation box). **f** Surface element compositions and optical photos of polysulfone (PSF) substrates with PIP only and with both PIP and LA adsorption. **g** Schematic diagrams of formation of control-TFC (C-TFC) and LA-TFC membranes with different morphological polyamide (PA) layer. **h** and **i** Free energy variations for the reactions between acyl chloride group of TMC and amine group of PIP/phenolic hydroxyl group of LA, respectively (the alkyl chain in LA molecule was deleted in order to let structure convergence during the calculation process). Error bars represent standard deviation of three independent measurements.
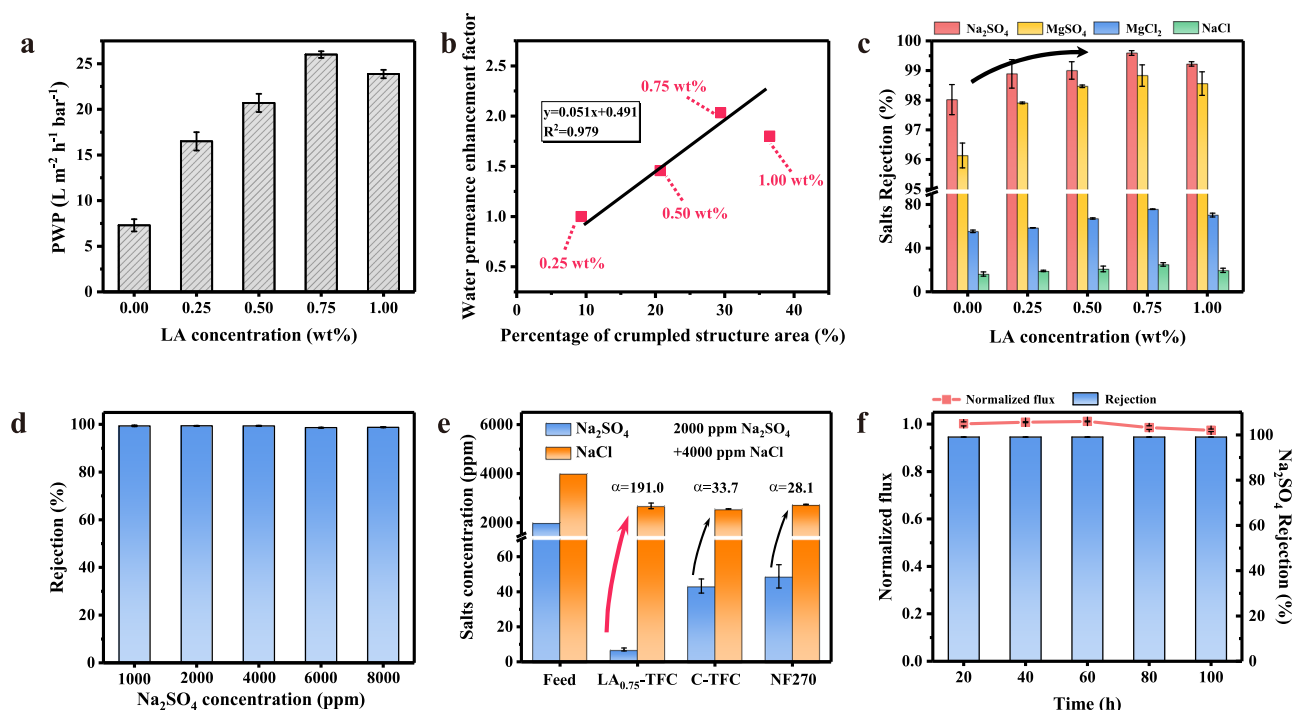
Fig. 4 | Separation performance of different thin film composite (TFC) membranes. a Effects of lignin alkali (LA) concentrations on pure water permeance (PWP) of LA-TFC membranes. **b** The correlation between water permeance enhancement factor and percentage of crumpled structure area of LA-TFC membranes. **c** Effects of LA concentrations on different salts rejections of LA-TFC membranes. **d** Na_2SO_4 rejections of $LA_{0.75}$-TFC at different Na_2SO_4 concentrations. **e** Na_2SO_4 and NaCl concentrations in the feed and permeant solutions and the selectivity factors (α) of NaCl to Na_2SO_4 of different TFC membranes. **f** Long-term separation performance of $LA_{0.75}$-TFC membrane. Error bars represent standard deviation of three independent measurements.

more effective filtration area. As observed by SEM, all LA-TFC membranes possessed a crumpled structure; furthermore, when the LA concentration was 0.75 wt%, these wrinkles were more abundant and uniformly distributed throughout the membrane surface (Supplementary Fig. 1). In contrast, when the LA concentration increased to 1.00 wt%, a stacked PA layer became apparently, which subsequently impeded water molecules transport and reduced water permeance. To gain a deeper comprehension of the impact of crumpled structure on the water permeance of LA-TFC membrane, the relationship between crumpled area percentage and water permeance enhancement factor was delved. Intriguingly, a linear correlation emerged between the water permeance enhancement factor and the ratio of crumpled area when utilizing LA with concentration below 0.75 wt% (Fig. 4b and Supplementary Information Fig. 15). This finding is consistent with the recent critical reviews on crumpled membrane that such structures can increase the effective water-transport area, which effectively increase the water permeance[20,38]. Tang and co-workers further modeled the effect of nanovoid contained in the crumpled structures on water permeance, revealing that the void containing membrane can potentially offer 1–2 orders of magnitude enhancement in permeance due to simultaneously increased filtration surface area and optimized transport pathways[39]. This demonstrates that an increasing proportion of well-distributed crumpled PA layer proves advantageous for enhancing membrane permeance. However, further increase in LA concentration to 1.00 wt% caused a reduction in the enhancement factor (Fig. 4b), possibly due to the extensive folding of the rejection layer (Supplementary Fig. 1e).

Figure 4c reveals that all the LA regulated TFC membranes exhibited higher salts rejections than those of C-TFC membrane ascribing to their denser PA layer with higher DNC (Supplementary Table 3). The MWCO measurement also proved this point. As shown in Supplementary Fig. 16, all the LA-TFC membranes had a smaller MWCO (~230 Da vs 282 Da) and narrower pore size distribution in comparison

with C-TFC membrane. For a typical PA NF membrane, the Donnan exclusion and sieving exclusion usually play crucial roles in the ion rejection. However, in this study, the streaming potential measurements (Supplementary Fig. 17a) show that the surface negative charge intensities of all LA-TFC membranes were weaker than that of C-TFC membrane under neutral pH condition. As above discussed, the LA molecules did not participate in IP reaction, thus the less negative charge intensities of LA-TFC membranes were attributed to the less carboxyl groups on their surface caused by the higher DNC of the PA layer (Supplementary Fig. 17b and Supplementary Table 3). Therefore, the increased salts rejections of LA-TFC membranes were mainly attributed to the highly cross-linked PA layer regulated by LA. Especially, when LA concentration was 0.75 wt%, the $LA_{0.75}$-TFC membrane showed the highest Na_2SO_4 rejection of 99.6%, while the C-TFC membrane presented a Na_2SO_4 rejection of 98.0%. Considering the PWP and salts rejections comprehensively, the optimal amount of LA was chosen at 0.75 wt%, thus the corresponding $LA_{0.75}$-TFC membrane was used in the following experiments.

In general, the salt rejection will decrease to a great degree when treating saline solution with higher salt concentration or operating under high pressure due to the intensified concentration polarization and shielding effect. In this study, the robustness of LA-TFC membrane under high saline condition or high operation pressure was also investigated. As shown in Fig. 4d, the $LA_{0.75}$-TFC membrane still maintained more than 99.2% Na_2SO_4 rejection at higher salt concentration, and similarly, it also showed stable Na_2SO_4 rejections under different operation pressures (Supplementary Fig. 18). To further assess its ion-ion selective ability, a simulated saline solution containing 2000 mg L^{-1} Na_2SO_4 and 4000 mg L^{-1} NaCl was employed as feed[40]. The results demonstrate that the $LA_{0.75}$-TFC membrane exhibited a prominent Cl^-/SO_4^{2-} selectivity factor ($\alpha = 191.0$), surpassing those of C-TFC ($\alpha = 33.7$) and commercial NF270 membranes ($\alpha = 28.1$) (Fig. 4e). Moreover, the $LA_{0.75}$-TFC membrane presented excellent long-term
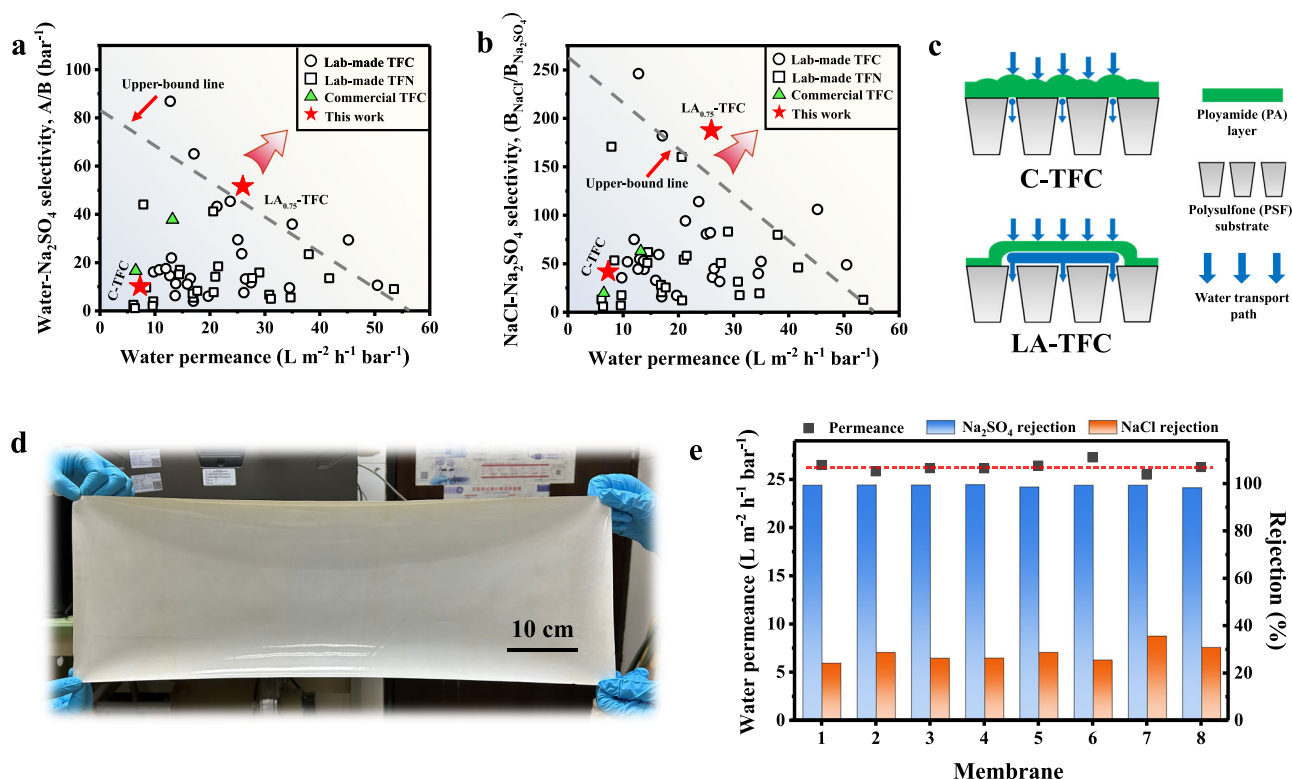
Fig. 5 | The performance comparison of lignin alkali$_{0.75}$ - thin film composite (LA$_{0.75}$-TFC, 0.75 represents the LA concentration of 0.75 wt%) membrane with most state-of-the-art membranes and its production potential. a, b Summary of water permeance as well as water/Na$_2$SO$_4$ and NaCl/Na$_2$SO$_4$ selectivities of polyamide (PA) nanofiltration (NF) membranes reported in literature and in market (detailed pure water permeance and salt rejection data were listed in Supplementary Table 5, and the water/Na$_2$SO$_4$ selectivity was calculated by Eq. (10)). **c** Schematic illustration of water permeance enhancement of LA-TFC membrane. **d** Optical photograph of the fabricated large size LA$_{0.75}$-TFC membrane. **e** Separation performances of membrane coupons selected from different positions of large size LA$_{0.75}$-TFC membrane corresponding to Supplementary Fig. 21.

separation stability during 100 h operation (Fig. 4f), and its surface remained intact after long-term operation as revealed by XPS and ATR-FTIR characterizations (Supplementary Fig. 19). Since LA can be available from alkaline paper pulp waste, we further investigated the possible use of real alkaline pulp wastewater as an additive of aqueous phase solution to fabricate TFC membrane. We obtained a black liquor primarily composed of LA from an alkaline pulping mill (Qingshan Paper Industry, Fu Jian, China) and used it as an additive in aqueous phase solution. The resultant NF membrane was denoted as BLA-TFC. The results show that the PWP of the BLA-TFC membrane reached 21.5 L m^{-2} h^{-1} bar^{-1}, which is almost three times that of C-TFC membrane. It also presented a high Na$_2$SO$_4$ rejection rate of 99.2% and a remarkable Cl$^-$/SO$_4^{2-}$ selectivity of 105 (Supplementary Fig. 20), which are superior to those of C-TFC and commercial NF270 membranes. Our study suggests the promising of LA or LA containing wastewater for fabricating TFC membranes for water softening, brine refining and other similar practical applications.

Furthermore, the PWP as well as selectivities of water/Na$_2$SO$_4$ and NaCl/Na$_2$SO$_4$ of LA$_{0.75}$-TFC membrane were compared with the state-of-the-art PA NF membranes reported in literature (Fig. 5a, b and Supplementary Table 5). Notably, the LA$_{0.75}$-TFC membrane possessed a higher Na$_2$SO$_4$ rejection and NaCl/Na$_2$SO$_4$ selectivity (191.0) without compromising water permeance. Its separation performance surpassed the upper-bound of most state-of-the-art PA NF membranes due to its ultrathin, highly cross-linked, and crumpled PA nanofilm (Fig. 5c). As above discussed, the ultrathin and crumpled PA nanofilm can decrease the water transport resistance and create more effective area for water collecting[38,39,41], thus endowing the LA-TFC membrane with higher PWP. Moreover, the highly cross-linked PA nanofilm exhibited a narrower pore size distribution, thus enhancing the

selectivity of LA-TFC membrane. Although there are many PA NF membranes with high-performance are fabricated by adding nanoadditives[40,42], or pre-conditioning of polymer/nanomaterial interlayers[13,14], the unavoidable problems such as agglomerated nanomaterials, extra carbon footprint, and lengthy operation steps hinder their commercialization. In contrast, the additive LA used in this work is abundant available from alkaline paper pulp waste, which will not create additional carbon footprint in membrane fabrication process, and the addition of LA in aqueous phase solution is compatible with the current manufacture line, easy to achieve commercialization.

In addition, considering that the practical application involves larger membrane area, we fabricated a large size LA$_{0.75}$-TFC membrane with dimensions of 65 cm × 25 cm to evaluate its actual production potential (Fig. 5d). Then, we selected eight membrane coupons from different positions (Supplementary Fig. 21) for separation performance test to assess its homogeneity. Encouragingly, these membrane coupons exhibited similar PWP (~26.3 L m^{-2} h^{-1} bar^{-1}) and Na$_2$SO$_4$ rejection (~99.3%) (Fig. 5e). The uniformity observed across various regions of this LA$_{0.75}$-TFC membrane suggests that it can be reliably employed for large-scale industrial applications without concerning about inconsistent performance or localized defects. This finding further supports the viability and potential widespread application of LA-regulated PA NF membrane for efficient filtration processes.

Discussion

We have proposed a simple and efficient approach that involves aqueous phase additive LA to regulate the distribution/diffusion rate of PIP and reaction rate of IP process for creating a robust NF membrane with an ultrathin, highly cross-linked, and crumpled PA separation layer. The as-developed NF membrane exhibited a high

pure water permeance of 26.0 L m^{-2} h^{-1} bar^{-1} with excellent Na$_2$SO$_4$ rejection of 99.6% and Cl$^-$/SO$_4^{2-}$ selectivity of 191.0, which was superior to the state-of-the-art TFC NF membranes reported in literature and in market. We also reveal that the percentage of crumpled structure on PA nanofilm has a strong relation to the water permeance enhancement, which can provide a refer to the further exploration and design of crumpled PA nanofilms. In addition, the additive LA used in this work is a resource from paper pulp waste, which will not create additional carbon footprint in membrane fabrication process. Moreover, the addition of LA in aqueous phase solution is compatible with the present industrial production line, and no additional steps are required during TFC membrane manufacturing. Furthermore, the abundant functional groups on LA molecule confer it a great potential to form composite materials, which can be used to develop membranes with special functions. For example, a kind of hydrogel fabricated based on LA-Ag nanocomposite possesses a long-term good cell affinity and high antibacterial property[43], which provides a possibility to the next generation environment-friendly antibacterial NF membrane fabrication.

Methods

Materials and chemical reagents
Materials and chemical reagents can be found in Supplement Experimental Methods 1.1.

Fabrication of different TFC membranes
The C-TFC membrane was fabricated by IP reaction in situ on a PSF UF substrate using an aqueous solution of 0.50 wt% PIP (pH 11.60) and a hexane solution of 0.15 wt% TMC. The PSF substrate was first fixed onto a customized plastic frame to make sure only the top surface was exposed to the solution. Then, 20 mL PIP solution was poured onto the substrate for 3 min. After PIP solution was drained out, an air knife was used to further remove the residue solution on the surface. Subsequently, the substrate was contacted with 20 mL TMC solution for 1 min followed by hexane rinsing for 5 s to remove unreacted TMC. Finally, the resulting C-TFC membrane was cured in an oven at 60 °C for 10 min to promote the cross-linking of PA network and then stored in DI water at 4 °C for further experiments.

The fabrication process of LA-TFC membrane was similar to that of C-TFC membrane as described above, except that a certain amount of LA (0.25, 0.50, 0.75, or 1.00 wt%) was added into the PIP solution. The pH values of the LA containing aqueous solutions were in the range of 11.56–11.41, which were similar with the control group without LA. The resulting membranes were denoted as LA$_n$-TFC membranes, where n represents the LA concentration. In order to explore the potential use of real alkaline pulp mill wastewater as an additive in aqueous solution for fabricating TFC NF membrane, a black liquor primarily containing LA was collected from an alkaline pulping mill (Qingshan Paper Industry, Fujian, China). The fabrication process was also similar with that of C-TFC membrane, and the resultant NF membrane was denoted as BLA-TFC. Prior to IP reaction, the black liquor was diluted 20 times to maintain the LA concentration the same as that used for fabricating LA$_{0.75}$-TFC membrane and added into 0.5 wt% PIP solution, and then the pH value of the aqueous solution was adjusted to 11.46 that similar with the LA containing aqueous solution (0.75 wt% of LA). No further purification steps were implemented.

Characterization of TFC membranes
ATR-FTIR (NEXUS 670, USA) and XPS (Thermo Scientific K-Alpha, USA) were used to analyze the surface chemical compositions of different membranes. SEM (Regulus 8230, Japan) was utilized to characterize membrane surface and cross-section morphologies. TEM (JEOL JEM-2100, Japan) and AFM (Dimension Fastscan, Bruker, USA) were

employed to observe the PA layer thickness and membrane surface roughness, respectively. The WCAs of different membranes were investigated on a goniometer (DSA25E, KRÜSS, Germany) based on sessile drop method. A streaming potential analyzer (SurPASS™ 3, Anton Paar, Austria) was utilized to ascertain the zeta potential values of membrane surfaces.

Separation performance of TFC membranes
The separation performances of TFC membranes were measured using a cross-flow filtration equipment (CF016D, Sterlitech, USA) with an effective filtration area of 16 cm^2. The PWP of TFC membranes was determined using deionized water as feed. All the membranes were pre-compacted at 5 bar for 30 min prior to permeate sample collection. Unless specified, the applied pressure, cross-flow velocity, and feed solution temperature were maintained at 5 bar, 0.1 m s^{-1}, and 25 °C, respectively. The PWP of the membranes was calculated by Eq. (1):

$$PWP = \frac{V}{\Delta P \times A \times T} \tag{1}$$

where PWP (L m^{-2} h^{-1} bar^{-1}) represents the pure water permeance of membrane, V (L) is the total volume of liquid permeating through membrane during filtration time T (h), ΔP (bar) is the applied pressure, and A (m^2) is the effective filtration area, respectively.

Single salt rejection of TFC membranes was evaluated using individual Na$_2$SO$_4$, MgSO$_4$, NaCl and MgCl$_2$ solution with concentration of 1000 mg L^{-1} as feed. The monovalent/divalent ion selectivity of TFC membranes was assessed using mixed salts solution with 2000 mg L^{-1} Na$_2$SO$_4$ and 4000 mg L^{-1} NaCl. The MWCO and pore size distribution of TFC membranes were determined by measuring the rejections of a series of neutral solutes (i.e., glycerol, glucose, sucrose, and raffinose) with concentration of 200 mg L^{-1}. The rejections of salts and neutral solutes were calculated by Eq. (2). The separation factor of NaCl to Na$_2$SO$_4$ (α) (both the mixed and single salt solutions) was calculated based on Eq. (3):

$$R = \left(1 - \frac{C_p}{C_f}\right) \times 100\% \tag{2}$$

$$\alpha = \frac{(C_{NaCl}/C_{Na_2SO_4})_p}{(C_{NaCl}/C_{Na_2SO_4})_f} = \frac{1 - R_{NaCl}}{1 - R_{Na_2SO_4}} \tag{3}$$

where R represents the salt or neutral solute rejection, C_p and C_f are the salt or neutral solute concentrations in permeate and feed solutions, respectively. The salt concentration was determined by measuring the solution conductivity using a conductivity meter (Mettler Toledo FE38, USA), the anion ion concentration in mixed salts solution was measured by ion chromatography (ICS-1100, ThermoFisher Scientific Co., Ltd., USA), and the neutral solute concentration was analyzed by a total organic carbon (TOC) analyzer (TOC-L, Shimadzu, Japan).

MD simulations
In the simulation of the aqueous phase bulk solution, a cubic simulation box with dimensions of 50 × 50 × 50 Å^3 was used, which contained 100 PIP molecules, 50 LA molecules, and 5000 water molecules. Radial distribution function (RDF) of PIP interaction with LA was analyzed in this model. The diffusion coefficient D of PIP in bulk solution was calculated using the mean square displacement (MSD) as a linear regression equation, given by Eqs. (4) and (5):

$$MSD(t) = \frac{1}{N} \sum_{j=1}^{N} [(r_j(t) - r_j(0))^2] \tag{4}$$

$$D = \frac{MSD(\text{t})}{6t} \tag{5}$$

Where $r_i(0)$ is the original positional coordinate of molecules/atoms, $r_i(t)$ is the position at time t, and N is the total number of molecular.

For simulating the water-hexane biphasic solution, a rectangular box with dimensions of $40 \times 40 \times 120\ \text{Å}^3$ was used to construct the system of hexane and LA/water mixture. The box was divided into three layers from bottom to top: hexane, LA/water mixture, and hexane. The hexane layers contained 150 hexane molecules, while the LA/water mixture layer contained 100 PIP molecules and 50 LA molecules.

All MD simulations were initialized using the Packmol software[44]. The water molecules were modeled using the three-site SPCE water model[45], and the atomic force field parameters were derived from the IL parameters of the OPLS-AA force field by Doherty et al.[46–48]. To avoid boundary effects, all simulations used three-dimensional periodic boundary conditions (PBC). The cut-off distance for non-bonded interactions was set to 12 Å, and the particle mesh Ewald (PME) method was used for long-range electrostatic interactions[49]. Before formal simulation, the system was pre-equilibrated using the steepest descent algorithm to remove excessive initial structural stress[50]. Subsequently, a 1 ns NPT simulation (with a time step of 2-fs) was conducted to equilibrate the system to its actual density. This was followed by a 10 ns formal NPT simulation with data collection performed using a 2-fs time step. Temperature and pressure coupling were achieved using the v-rescale thermostat and Berendsen barostat, respectively, at 298.15 K and 1 atm[51,52]. All MD simulations were performed using GROMACS 2018.8[53], and all visualized structures were provided by VMD 1.9.4 54[54].

For calculating the free energy change of PIP crossing the aqueous-organic interface, a two-layer simulation box with dimensions of $40 \times 40 \times 100\ \text{Å}^3$ was constructed. The LA/water mixture and hexane occupied the regions $z < 50\ \text{Å}$ and $z > 50\ \text{Å}$, respectively. A PIP molecule was placed in the aqueous phase with its center of mass coordinates at (20 Å, 20 Å, 30 Å). Prior to sampling, energy minimization was performed, followed by 1 ns pre-equilibration under NPT conditions using Berendsen pressure control[51], with position restraints applied to the PIP molecule. Subsequently, stretching MD simulations were conducted under NPT conditions, which stretch the PIP molecule by 4 nm along the Z-axis to cross the aqueous-organic interface. 20 configurations were selected from the simulation trajectories at regular time intervals. Each configuration underwent 1 ns of NPT pre-equilibration and 2 ns of umbrella sampling simulations. The reaction coordinate was defined as the projection of the center of mass coordinates for PIP onto the pulling vector. To determine the free energy distribution of PIP interfacial diffusion, we employed the weighted histogram analysis method (WHAM) to analyze the average force along the reaction coordinate[55]. In the results of final free energy change, we set the aqueous-organic interface as the origin point and took 1.5 nm in the direction of the aqueous phase and the organic phase to collect the simulated data for analysis.

Density functional theory calculations

Geometry optimizations and harmonic vibrational frequency calculations were performed on PIP, LA, and TMC using DFT methods with the B3LYP hybrid functional[56] and the 6-311G(d,p) basis[57] sets in Gaussian 16 software[58]. To consider solvation effects, SMD's polarizable continuum solvent model was utilized[59]. Stable minima without imaginary frequencies or transition states with only one imaginary frequency were identified as stationary points. The reported energies included a zero-point energy correction. The binding energies were calculated based on Eq. (6). The reaction free energy barrier was calculated using Eq. (7):

$$E_{\text{binding}} = E_{x+pip} - E_x - E_{pip} \tag{6}$$

$$\Delta G = G_{TS} - G_R \tag{7}$$

where E_{x+pip} represents the total energy of the system with both PIP and PSF or PIP and LA, E_x is the energy of the system without PIP, E_{pip} is the energy of PIP, and G_R and G_{TS} represent the Gibbs free energies of reactant and transition state, respectively.

UV spectrophotometer characterization

The partitioned amount of PIP into blank hexane was measured by UV spectrometer (UNICO-UV2, China). Specifically, 5 mL of 0.5 wt% PIP solution (with or without addition of LA) was first placed in the sample bottle, and then 5 mL of pure hexane was slowly added. After 1 min PIP diffusion at 25 °C, 2 mL of the above hexane solution near the aqueous-organic interface was collected with a pipette, and the PIP absorbance was tested at the maximum characteristic peak 208 nm. The partition coefficient K_d of PIP in organic and aqueous phases can be calculated by Eq. (8)[60]:

$$K_d = \frac{C_O \times V_O}{C_W \times V_W - C_O \times V_O} \tag{8}$$

Where V_W and V_O are the volume of the aqueous phase and organic phase solutions, respectively; C_W represents the PIP concentration in the aqueous phase at the initial time; C_O represents the PIP concentration in the organic phase.

To in situ monitor the diffusion rate of PIP into the organic phase, 0.9 mL of 0.5 wt% PIP solution (with or without addition of LA) was first carefully added into the bottom of a quartz cuvette. Then, 0.5 mL of pure hexane was gently added on top of PIP layer. The PIP absorbance in hexane was tested at the maximum characteristic peak 208 nm and recorded at every 1 s time interval for 120 s.

The consumption rate of TMC in organic phase was used to reflect the IP reaction rate. To in situ monitor the consumption of TMC in organic phase, 0.9 mL of 0.5 wt% PIP aqueous solution (with or without addition of LA) was first carefully added into the bottom of a quartz cuvette. Then, 0.5 mL hexane with 0.05 wt% TMC was then gently added on top of PIP layer. The TMC absorbance in hexane was tested at the maximum characteristic peak 290 nm and recorded at every 1 s time interval for 120 s.

Calculation of water permeance enhancement factors

The water permeance enhancement factors of LA-TFC membranes were calculated by Eq. (9):

$$E = \frac{P_i - P_0}{P_{0.25} - P_0} \times 100\% \tag{9}$$

where E represents the water permeance enhancement factor; P_O and P_i are the pure water permeance of C-TFC and LA-TFC membranes, respectively, and the subscript i represents the LA concentration varying from 0.25 to 1.00 wt%.

The water/salt permselectivity

According to solution-diffusion model, the water/salt permselectivity can be calculated by Eq. (10):

$$R = \frac{\frac{A}{B}(\Delta P - \Delta \pi)}{\frac{A}{B}(\Delta P - \Delta \pi) + 1} \tag{10}$$

where R is the salt rejection, A is the pure water permeability, B is the salt permeability, ΔP is the operation pressure, and $\Delta \pi$ is the osmotic pressure difference across the membrane[61].

Data availability

All data in the manuscript or the supplementary information are available from the corresponding authors. Source data are provided with this paper.

References

1. Mauter, M. S. et al. The role of nanotechnology in tackling global water challenges. *Nat. Sustain.* **1**, 166–175 (2018).
2. Lu, D. et al. Separation mechanism, selectivity enhancement strategies and advanced materials for mono-/multivalent ion-selective nanofiltration membrane. *Adv. Membr.* **2**, 100032 (2022).
3. Tang, C. Y. et al. Potable Water reuse through advanced membrane technology. *Environ. Sci. Technol.* **52**, 10215–10223 (2018).
4. Karan, S., Jiang, Z. & Livingston, A. G. Sub–10 nm polyamide nanofilms with ultrafast solvent transport for molecular separation. *Science* **348**, 1347–1351 (2015).
5. Lu, X. & Elimelech, M. Fabrication of desalination membranes by interfacial polymerization: history, current efforts, and future directions. *Chem. Soc. Rev.* **50**, 6290–6307 (2021).
6. Ben-Zvi, A., Taqui, U., Ramon, G. & Nunes, S. P. Alternative materials for interfacial polymerization: recent approaches for greener membranes. *Green Chem.* **26**, 6237–6260 (2024).
7. Xu, Y. et al. Enhanced water permeability in nanofiltration membranes using 3D accordion-like MXene particles with random orientation of 2D nanochannels. *J. Mater. Chem. A* **10**, 16430–16438 (2022).
8. Zhang, R., Tian, J., Gao, S. & Van der Bruggen, B. How to coordinate the trade-off between water permeability and salt rejection in nanofiltration? *J. Mater. Chem. A* **8**, 8831–8847 (2020).
9. Sarkar, P., Modak, S. & Karan, S. Ultraselective and highly permeable polyamide nanofilms for ionic and molecular nanofiltration. *Adv. Funct. Mater.* **31**, 2007054 (2021).
10. Liang, Y. et al. Polyamide nanofiltration membrane with highly uniform sub-nanometre pores for sub-1 Å precision separation. *Nat. Commun.* **11**, 2015 (2020).
11. Jiang, Z., Karan, S. & Livingston, A. G. Water transport through ultrathin polyamide nanofilms used for reverse osmosis. *Adv. Mater.* **30**, 1705973 (2018).
12. Zhu, J. et al. Rapid water transport through controllable, ultrathin polyamide nanofilms for high-performance nanofiltration. *J. Mater. Chem. A* **6**, 15701–15709 (2018).
13. Zhang, X., Lv, Y., Yang, H.-C., Du, Y. & Xu, Z.-K. Polyphenol coating as an interlayer for thin-film composite membranes with enhanced nanofiltration performance. *ACS Appl. Mater. Interfaces* **8**, 32512–32519 (2016).
14. Yang, Z. et al. Tannic acid/Fe^{3+} nanoscaffold for interfacial polymerization: toward enhanced nanofiltration performance. *Environ. Sci. Technol.* **52**, 9341–9349 (2018).
15. Zhu, X. et al. Ultrathin thin-film composite polyamide membranes constructed on hydrophilic poly (vinyl alcohol) decorated support toward enhanced nanofiltration performance. *Environ. Sci. Technol.* **54**, 6365–6374 (2020).
16. Zhao, C. et al. Polyamide membranes with nanoscale ordered structures for fast permeation and highly selective ion-ion separation. *Nat. Commun.* **14**, 1112 (2023).
17. Smith, R. A. et al. Neighboring parenchyma cells contribute to Arabidopsis xylem lignification, while lignification of interfascicular fibers is cell autonomous. *Plant Cell* **25**, 3988–3999 (2013).
18. Smith, R. A. et al. Defining the diverse cell populations contributing to lignification in Arabidopsis stems. *Plant Physiol.* **174**, 1028–1036 (2017).
19. Sun, W. et al. Bioinspired lignin-based loose nanofiltration membrane with excellent acid, fouling, and chlorine resistances toward dye/salt separation. *J. Membr. Sci.* **670**, 121372 (2023).
20. Shao, S. et al. Nanofiltration membranes with crumpled polyamide films: a critical review on mechanisms, performances, and environmental applications. *Environ. Sci. Technol.* **56**, 12811–12827 (2022).
21. Wong, M. C. Y., Lin, L., Coronell, O., Hoek, E. M. V. & Ramon, G. Z. Impact of liquid-filled voids within the active layer on transport through thin-film composite membranes. *J. Membr. Sci.* **500**, 124–135 (2016).
22. Wang, Z. et al. Nanofiltration membranes with octopus arm-sucker surface morphology: filtration performance and mechanism investigation. *Environ. Sci. Technol.* **55**, 16676–16686 (2021).
23. Lai, G. S. et al. Tailor-made thin film nanocomposite membrane incorporated with graphene oxide using novel interfacial polymerization technique for enhanced water separation. *Chem. Eng. J.* **344**, 524–534 (2018).
24. Park, S.-J. et al. Fabrication of polyamide thin film composite reverse osmosis membranes via support-free interfacial polymerization. *J. Membr. Sci.* **526**, 52–59 (2017).
25. Habib, S., Larson, B. E. & Weinman, S. T. Effect of surfactant structure on MPD diffusion for interfacial polymerization. *J. Membr. Sci. Lett.* **3**, 100055 (2023).
26. Nulens, I., Zvi, A. B., Vankelecom, I. F. J. & Ramon, G. Z. Re-thinking polyamide thin film formation: How does interfacial destabilization dictate film morphology? *J. Membr. Sci.* **656**, 120593 (2022).
27. Peng, L. E., Yao, Z., Yang, Z., Guo, H. & Tang, C. Y. Dissecting the role of substrate on the morphology and separation properties of thin film composite polyamide membranes: seeing is believing. *Environ. Sci. Technol.* **54**, 6978–6986 (2020).
28. Ben-Zvi, A. M. & Ramon, G. Z. Hydrodynamic instability triggered during thin-film formation by interfacial polymerization. *Phys. Fluids.* **36**, 092104 (2024).
29. Li, X. et al. Regulating the interfacial polymerization process toward high-performance polyamide thin-film composite reverse osmosis and nanofiltration membranes: a review. *J. Membr. Sci.* **640**, 119765 (2021).
30. Wen, Y. et al. Metal-organic framework enables ultraselective polyamide membrane for desalination and water reuse. *Sci. Adv.* **8**, eabm4149 (2022).
31. Wang, D. et al. Thin-film composite membranes interlayered with amphiphilic MoS$_2$ nanosheets via controllable interfacial polymerization for enhanced desalination performance. *Environ. Sci. Technol.* **58**, 11855–11863 (2024).
32. Zhu, C.-Y. et al. Polyamide nanofilms with linearly-tunable thickness for high performance nanofiltration. *J. Membr. Sci.* **627**, 119142 (2021).
33. Jimenez-Solomon, M. F., Song, Q., Jelfs, K. E., Munoz-Ibanez, M. & Livingston, A. G. Polymer nanofilms with enhanced microporosity by interfacial polymerization. *Nat. Mater.* **15**, 760–767 (2016).
34. Karami, P. et al. Novel lignosulfonated polyester membranes with remarkable permeability and antifouling characteristics. *J. Membr. Sci.* **687**, 122034 (2023).
35. Zheng, J. et al. Separation of textile wastewater using a highly permeable resveratrol-based loose nanofiltration membrane with excellent anti-fouling performance. *Chem. Eng. J.* **434**, 134705 (2022).
36. Bai, Y. et al. Microstructure optimization of bioderived polyester nanofilms for antibiotic desalination via nanofiltration. *Sci. Adv.* **9**, eadg6134 (2023).
37. Freger, V. & Ramon, G. Z. Polyamide desalination membranes: formation, structure, and properties. *Prog. Polym. Sci.* **122**, 101451 (2021).
38. Gan, Q. et al. Nanofoamed polyamide membranes: mechanisms, developments, and environmental implications. *Environ. Sci. Technol.* **58**, 20812–20829 (2024).
39. Hu, Y., Wang, F., Yang, Z. & Tang, C. Y. Modeling nanovoid-enhanced water permeance of thin film composite membranes. *J. Membr. Sci.* **675**, 121555 (2023).
40. Han, S. et al. Microporous organic nanotube assisted design of high performance nanofiltration membranes. *Nat. Commun.* **13**, 7954 (2022).
41. Tan, Z., Chen, S., Peng, X., Zhang, L. & Gao, C. Polyamide membranes with nanoscale Turing structures for water purification. *Science* **360**, 518–521 (2018).

42. Zhu, J. et al. MOF-positioned polyamide membranes with a fishnet-like structure for elevated nanofiltration performance. *J. Mater. Chem. A* **7**, 16313–16322 (2019).

43. Gan, D. et al. Plant-inspired adhesive and tough hydrogel based on Ag-Lignin nanoparticles-triggered dynamic redox catechol chemistry. *Nat. Commun.* **10**, 1487 (2019).

44. Martínez, L., Andrade, R., Birgin, E. G. & Martínez, J. M. PACKMOL: A package for building initial configurations for molecular dynamics simulations. *J. Comput. Chem.* **30**, 2157–2164 (2009).

45. Horn, H. W. et al. Development of an improved four-site water model for biomolecular simulations: TIP4P-Ew. *J. Chem. Phys.* **120**, 9665–9678 (2004).

46. Jorgensen, W. L., Maxwell, D. S. & Tirado-Rives, J. Development and testing of the OPLS all-atom force field on conformational energetics and properties of organic liquids. *J. Am. Chem. Soc.* **118**, 11225–11236 (1996).

47. Sambasivarao, S. V. & Acevedo, O. Development of OPLS-AA force field parameters for 68 unique ionic liquids. *J. Chem. Theory Comput.* **5**, 1038–1050 (2009).

48. Doherty, B., Zhong, X., Gathiaka, S., Li, B. & Acevedo, O. Revisiting OPLS force field parameters for ionic liquid simulations. *J. Chem. Theory Comput.* **13**, 6131–6145 (2017).

49. Darden, T., York, D. & Pedersen, L. Particle mesh Ewald: an N· log (N) method for Ewald sums in large systems. *J. Chem. Phys.* **98**, 10089–10092 (1993).

50. Payne, M. C., Teter, M. P., Allan, D. C., Arias, T. A. & Joannopoulos, A. J. D. Iterative minimization techniques for ab initio total-energy calculations: molecular dynamics and conjugate gradients. *Rev. Mod. Phys.* **64**, 1045 (1992).

51. Berendsen, H. J. C., Postma, J. P. M. V., Van Gunsteren, W. F., DiNola, A. & Haak, J. R. Molecular dynamics with coupling to an external bath. *J. Chem. Phys.* **81**, 3684–3690 (1984).

52. Bussi, G., Donadio, D., & Parrinello, M. Canonical sampling through velocity rescaling. *J. Chem. Phys.* **126**, 014101 (2007).

53. Abraham, M. J. et al. GROMACS: High performance molecular simulations through multi-level parallelism from laptops to supercomputers. *SoftwareX* **1**, 19–25 (2015).

54. Humphrey, W., Dalke, A. & Schulten, K. VMD: visual molecular dynamics. *J. Mol. Graph.* **14**, 33–38 (1996).

55. Kumar, S., Rosenberg, J. M., Bouzida, D., Swendsen, R. H. & Kollman, P. A. The weighted histogram analysis method for free-energy calculations on biomolecules. I. The method. *J. Comput. Chem.* **13**, 1011–1021 (1992).

56. Stephens, P. J., Devlin, F. J., Chabalowski, C. F. & Frisch, M. J. Ab initio calculation of vibrational absorption and circular dichroism spectra using density functional force fields. *J. Phys. Chem. C.* **98**, 11623–11627 (1994).

57. Frisch, M. J., Pople, J. A. & Binkley, J. S. Self-consistent molecular orbital methods 25. Supplementary functions for Gaussian basis sets. *J. Chem. Phys.* **80**, 3265–3269 (1984).

58. Frisch, M. J. et al. *Gaussian 16 Rev. C.01*. Wallingford, CT (2016).

59. Marenich, A. V., Cramer, C. J. & Truhlar, D. G. Universal solvation model based on solute electron density and on a continuum model of the solvent defined by the bulk dielectric constant and atomic surface tensions. *J. Phys. Chem. B* **113**, 6378–6396 (2009).

60. Wang, Z., Liang, S., Jin, Y., Zhao, L. & Hu, L. Controlling structure and properties of polyamide nanofilms by varying amines diffusivity in organic phase. *J. Membr. Sci.* **574**, 1–9 (2019).

61. Yang, Z., Guo, H. & Tang, C. Y. The upper bound of thin-film composite (TFC) polyamide membranes for desalination. *J. Membr. Sci.* **590**, 117297 (2019).

Author contributions
W.T.Z. and S.S.Z. proposed the idea, designed the research, and supervised the project. W.T.Z., H.Y.L. and C.X.L. performed experiments, including membrane fabrication, characterization and analyses, and membrane separation performance measurements. W.T.Z. drew the figures and wrote the manuscript. W.T.Z., S.W.Z., and W.W. performed DFT calculations and MD simulations. S.S.Z., C.Y.T., and F.G.M. received the funds, participated in discussion, and revised the manuscript. All authors contributed to the drafting and revising the manuscript.

Competing interests
The authors declare no competing interest.

Additional information
Supplementary information The online version contains supplementary material available at https://doi.org/10.1038/s41467-024-55595-y.

Correspondence and requests for materials should be addressed to Shanshan Zhao, Chuyang Y. Tang or Fangang Meng.

Peer review information *Nature Communications* thanks Yoshito Ando, Akshay Deshmukh and the other, anonymous, reviewer(s) for their contribution to the peer review of this work. A peer review file is available.

Reprints and permissions information is available at http://www.nature.com/reprints

Publisher's note Springer Nature remains neutral with regard to jurisdictional claims in published maps and institutional affiliations.